DIFFUSION-BASED SPATIO-TEMPORAL INTERPOLATION WITH DYNAMIC SENSOR SETS

Anonymous authors
Paper under double-blind review

ABSTRACT

We tackle spatio-temporal interpolation for virtual sensors in sparse, partially observed, and dynamically changing networks. We introduce DynaSTI, a diffusion-based generative framework that is fully inductive to unseen locations, trains directly on incomplete observations, and remains effective without retraining when sensor networks change with time. Our contributions are threefold: (i) a unified conditioning strategy that yields calibrated predictive distributions and robust performance under severe input-sensor dropout; (ii) a Fourier-domain compression variant, FDynaSTI, that accelerates sampling performance, and (iii) state-of-the-art performance on multiple real-world datasets, improving both RMSE and CRPS relative to strong baselines. Together, these results establish diffusion-based, frequency-aware probabilistic interpolation as a scalable solution for real-world, dynamic sensor networks.

1 INTRODUCTION

Accurate modeling and interpolation of spatio-temporal signals underpin a wide range of practical applications, including environmental monitoring, traffic analysis, and urban planning. A particularly challenging yet important task within this domain is predicting multivariate time-series data at locations devoid of sensors or historical observations, commonly termed as virtual sensors. This process, known as spatio-temporal interpolation, is essential for enabling informed decision making in scenarios where sensor networks are sparse, incomplete, or subject to dynamic changes. Our primary objective is to develop a robust method that accurately predicts data for these unseen locations without requiring prior knowledge of their coordinates during training. Our model is specifically engineered to handle sensor networks that change over time, while assuming only that the underlying observation distribution remains stationary.

Classical approaches such as kriging/Gaussian processes (Matheron, 1963; Cressie, 1993; Rasmussen & Williams, 2006; Hamelijnck et al., 2021), ARMA/VAR models (Box & Jenkins, 1990), EM-based matrix/tensor completion (Dempster et al., 1977), and spatial statistics provide principled uncertainty but often rely on strong stationarity assumptions, hand-crafted kernels, dense coverage, and fixed topologies; they also struggle to scale to large, high-dimensional networks. More recent deep methods—graph neural networks (Cini et al., 2022; Tharzeen et al., 2023; Yang et al., 2025; Kuppannagari et al., 2021), attention-based sequence models (Marisca et al., 2022; Nie et al., 2024), neural processes (Hu et al., 2023), and diffusion-based imputers (Liu et al., 2023; Hu et al., 2024; Tashiro et al., 2021; Islam et al., 2025)–have improved expressivity and accuracy on partially observed data, yet commonly presume that the set of observed and target sensors and their graph/topology are fixed at training and test time. Moreover, uncertainty quantification for unseen locations is frequently ad hoc (e.g., MC-dropout (Gal & Ghahramani, 2016)) or absent, and many models require costly retraining or architectural change when the sensors drop out. In summary, no existing approach simultaneously supports dynamic sensor configurations, long sequences, multivariate data, and uncertainty prediction for virtual sensors.

To address these challenges, we propose a novel diffusion-based generative framework for spatio-temporal interpolation that leverages spatial, temporal, and feature encoders. Our model, *DynaSTI*, short for "**Dyna**mic **S**patio-**T**emporal **I**nterpolation via Diffusion", is specifically engineered to predict multivariate time-series data at virtual sensor locations, excelling in scenarios where input sensor data may be incomplete or missing at training and testing time. Moreover, Our model eliminates

Table 1: Comparison of spatio-temporal interpolation methods by key strengths.

Strength	GRIN	ST-GAIN	SPIN	PriSTI	IGNNK	DeepKriging	ST-VGP	KITS	GSLI	BayesNF	MMGN	USTD	ImputeFormer	DynaSTI
Dynamic Topology					✓		✓	✓	✓	✓	✓	✓		✓
Inductive					✓	✓	✓	✓	✓	✓	✓	✓		✓
Generative		✓		✓			✓			✓	✓	✓		✓
Multivariate	✓	✓	✓	✓	✓	✓	✓	✓	✓			✓	✓	✓
Incomplete inputs	✓	✓	✓	✓	✓			✓	✓	✓	✓	✓	✓	✓

the need for retraining when sensor configurations change, is fully inductive to unseen locations, uses a unified conditioning scheme to ingest whatever sensors are available, naturally represents uncertainty, and accelerates long-horizon inference through a Fourier-domain compression–together yielding a scalable, and cost-effective solution.

Table 1 summarizes how various models for spatio-temporal interpolation address four critical strengths relevant to virtual sensor prediction – (1) **Dynamic Topology**, which is adaptability to sensor networks whose configuration changes dynamically (e.g., sensors being added or removed), (2) **Inductive** is the ability to predict at locations unseen during training, (3) **Generative** is to providing probabilistic outputs rather than solely deterministic predictions, (4) **Multivariate** is the ability to predict for multivariate data instead of just univariate, and (5) **Incomplete inputs** is the ability to handle incomplete data with arbitrary missing feature values as input at training and testing time. While USTD (Hu et al., 2024) meets all criteria in Table 1, the public implementation restricts sequences to 12 or 24 steps, so we were unable to run it on our datasets, which have longer sequences.

Our key contributions are:

- **Inductive diffusion for virtual sensors:** We propose a fully inductive, diffusion-based framework that trains directly on incomplete data and generalizes to unseen target locations without retraining.
- **Unified conditioning with locations and probabilistic prediction:** We introduce a conditioning strategy that integrates irregular spatio-temporal context (locations) into the denoising process, delivering robust performance under severe sensor dropout. The approach produces probabilistic predictions yielding uncertainty quantification.
- **Fourier-domain compression for long sequences:** We develop a frequency-aware representation that expresses each series as a trend (intercept + slope) and seasonality to accelerate the inference time.
- **Strong empirical performance and robustness:** Across diverse, real-world datasets, DynaSTI achieves state-of-the-art accuracy relative to strong baselines (e.g., lower RMSE and improved CRPS) and shows graceful degradation with sensor dropout.

2 Related Work

Traditional statistical approach: Classical methods—ARMA (Box & Jenkins, 1990), EM (Dempster et al., 1977), and KNN (Fix & Hodges, 1951)—leverage temporal smoothness or spatial similarity but miss complex dependencies. Kriging (Matheron, 1963; Cressie, 1993) and Gaussian Processes (GPs) (Rasmussen & Williams, 2006; Cressie & Wikle, 2011) provide principled uncertainty via covariance kernels, yet suffer from cubic scaling and sensitivity to stationarity/kernel choice.

Deterministic deep models: Graph-based models (GRIN (Cini et al., 2022), GLSTM (Tharzeen et al., 2023), STGNN-DAE (Kuppannagari et al., 2021)) capture spatial–temporal structure but typically assume fixed topologies and can accumulate autoregressive errors in sparse regimes. GSLI (Yang et al., 2025) learns multi-scale graphs to handle node/feature heterogeneity but adds compute overhead. Attention models like SPIN (Marisca et al., 2022) enable virtual prediction with local representations but require known locations during training. Other deterministic methods–tensor completion (Ben Said & Erradi, 2022; Zhang & Wei, 2024), MLP-RAIN (Saubhagya et al., 2024), and image inpainting Yun et al. (2023)–work well on grids yet adapt poorly to irregular/dynamic graphs and usually lack calibrated uncertainty. Inductive kriging with GNNs (IGNNK (Wu et al., 2021), DeepKriging (Nag et al., 2023), INCREASE (Zheng et al., 2023), KITS (Li et al., 2023)) generalizes to unseen nodes but often simplifies temporal dynamics, may depend on side information, or rely on pseudo-labels. INR-style continuous fields (MMGN) (Luo et al., 2024) learns coordinate-to-value mappings but is deterministic and lacks explicit graph inductive bias. STFNN (Feng et al., 2024) models air-quality data as a continuous spatio-temporal field, learning its gradient with implicit neural representations and refining predictions through Pyramidal Inference to capture both low- and high-frequency patterns. Casper (Jing et al., 2024) introduces a causality-aware STGNN that uses frontdoor adjustment, a Prompt-Based Decoder, and Spatiotemporal Causal Attention to mitigate spurious correlations and learn sparse causal relations.

Probabilistic methods: Probabilistic approaches quantify uncertainty: STGNP (Hu et al., 2023) (neural processes on graphs) relies on predefined graphs/covariates. Bayesian Neural Fields (Saad et al., 2024) scale via hierarchical inference but approximate posteriors. ST-VGP (Hamelijnck et al., 2021) uses variational/state-space structure for linear-time scaling with assumptions on kernels/likelihoods. ST-GAIN (Zhang et al., 2017) is a GAN-based imputation model, which suffers from the training instability of GANs. Diffusion models handle nonstationarity generatively: CSDI (Tashiro et al., 2021) and SADI (Islam et al., 2025) impute time series without spatial context; PriSTI (Liu et al., 2023) adds spatio-temporal conditioning but remains non-inductive; USTD (Hu et al., 2024) unifies forecasting/kriging with a shared encoder and gated-attention decoders, supports inductive kriging but is evaluated on fixed training graphs and short sequences; VDM (Li et al., 2026) combines VAE pre-imputation, multi-scale trends, and temporal Mamba (Gu & Dao, 2024) with dynamic/static graph encoders, assuming a fixed distance graph and risking VAE bias.

3 Preliminaries

In this section, we first outline our problem setup and then provide an overview of the diffusion model concepts that are relevant to our approach.

3.1 Problem setup

We tackle spatio-temporal interpolation, predicting target time-series at arbitrary locations from multivariate sensors with missing and time-varying observations. This reflects real deployments (digital agriculture, atmospheric sensing) where sparse networks face outages and changing topologies. Our goal is a single model that generalizes across variables, time intervals, and virtual locations using the available sensor data.

More formally, a spatio-temporal dataset consists of sensor observations indexed by location and time. We let $\mathcal{S}$ denote the set of possible spatial coordinates, which will typically be 2D or 3D geographic locations, and $\mathcal{S}'$ denote the finite set of locations involved in the data under consideration. We consider a discrete time model where $\mathcal{T} = \{t_1, t_2, \ldots, t_T\}$ is the set of regularly sampled time steps spanning the temporal extent of the data. We consider multivariate sensors with C channels that produce data of the form $(s, t, \mathbf{x}, \mathbf{m})$, indicating the sensor location $s \in \mathcal{S}'$, the measurement time $t \in \mathcal{T}$, sensor values $\mathbf{x} \in \mathbb{R}^C$, and a channel mask $\mathbf{m} \in \{0,1\}^C$, indicating which channels are missing (0 indicates missing). Importantly, we make no assumptions about how many missing values are in the data at either training or testing time. The observed dataset is defined as:

$$\mathcal{D} = \big\{(s, t, \mathbf{x}, \mathbf{m}) \;\big|\; s \in \mathcal{S}', t \in \mathcal{T}, \mathbf{x} \in \mathbb{R}^C, \mathbf{m} \in \{0,1\}^C, \text{ where } m_c = 1 \text{ if } x_c \text{ is observed, else } 0\big\}$$

The goal of spatio-temporal interpolation is to estimate one or more unobserved sensor channels at an arbitrary location s^* and all time steps $\mathcal{T}$ using a dataset of observed data $\mathcal{D}$. This process handles situations where some channel values are observed at s^*, with a mask $M^* \in \{0,1\}^{T \times C}$, which indicates which features/channels in $X^* \in \mathbb{R}^{T \times C}$ are missing for any time and are to be estimated as the data at the target location can be partially observed. For virtual locations, the mask M^* is all zeros and the goal is to predict the entire time-series data at the location s^*.

3.2 Diffusion models

Diffusion models provide a generative framework for sampling from complex data distributions. They define a *forward diffusion* process that incrementally adds noise to data, and a *reverse denoising* process that learns to remove this added noise. Concretely, let $X_0 \sim q(X_0)$ be a sample from the true data distribution. The forward diffusion process is a fixed Markov chain:

$$q\big(X_k \mid X_{k-1}\big) = \mathcal{N}\Big(X_k;\, \sqrt{1-\beta_k}\, X_{k-1},\, \beta_k \mathbf{I}\Big), \quad k = 1, \ldots, K,$$

where β_k is a variance schedule and $\mathbf{I}$ is the identity matrix. After K steps, X_K is nearly isotropic Gaussian noise.

A *reverse diffusion* model p_θ parameterized by θ is then trained to reconstruct X_0 from X_K via:

$$p_\theta\big(X_{k-1} \mid X_k\big) = \mathcal{N}\big(X_{k-1};\, \boldsymbol{\mu}_\theta(X_k, k),\, \boldsymbol{\Sigma}_\theta(X_k, k)\big).$$

Sampling from the trained model amounts to starting from Gaussian noise $X_K \sim \mathcal{N}(0, \mathbf{I})$ and iteratively applying the learned reverse steps:

$$X_{k-1} \sim p_\theta\big(X_{k-1} \mid X_k\big), \quad k = K, K-1, \ldots, 1.$$

A popular way to train the reverse diffusion model is via *noise prediction*. Let $\bar{\alpha}_k = \prod_{\ell=1}^{k}(1 - \beta_\ell)$. We construct X_k by mixing the clean sample X_0 with Gaussian noise ε:

$$X_k = \sqrt{\bar{\alpha}_k}\, X_0 \; + \; \sqrt{1 - \bar{\alpha}_k}\, \varepsilon, \quad \varepsilon \sim \mathcal{N}(0, \mathbf{I}).$$

The model p_θ (often denoted ε_θ) directly predicts ε. This yields a simple mean-squared error objective according to Ho et al. (2020):

$$\mathcal{L}(\theta) = \mathbb{E}_{x_0 \sim q,\ \varepsilon \sim \mathcal{N}(0,\mathbf{I}),\ k \sim \text{Uniform}\{1,\ldots,K\}} \Big[\big\|\varepsilon - \varepsilon_\theta(X_k, k)\big\|^2 \Big].$$

Minimizing this loss encourages ε_θ to correctly denoise X_k at each step k. By integrating conditional mechanisms into ε_θ, these models can be adapted for *conditioned generation*, making them suitable for tasks such as spatio-temporal interpolation. In such a setup, the model conditions on partial observations (spatial locations, diffusion steps, known features) and generates the missing values accordingly.

4 Dynamic Spatio-temporal Data Interpolation

We propose DynaSTI, a DDPM-based (Ho et al., 2020) framework for multivariate spatio-temporal interpolation that predicts time series at virtual sensor locations without prior coordinate knowledge. It conditions noise prediction on observed measurements, sensor coordinates, and the diffusion step–naturally handling missing data and dynamic topologies. The denoiser comprises three modules: Spatial, Temporal, and Feature Encoders that capture spatial correlations, long-range temporal dependencies, and cross-channel interactions, respectively (Fig. 1).

4.1 Model overview

Our model operates within the DDPM framework, where a forward diffusion process incrementally adds Gaussian noise to the data, and a reverse denoising process learns to reconstruct the original data distribution. For spatio-temporal interpolation, we aim to estimate multivariate time-series data $X^* \in \mathbb{R}^{T \times C}$ at a target location $s^* \in \mathbb{R}^d$ and time steps $\mathcal{T}$, conditioned on observed measurements $\mathcal{D}$ (See Section 3.1). The denoising model ε_θ estimates the noise ε added to the target data, conditioned on the noisy target data $X_k^* \in \mathbb{R}^{T \times C}$, the target location s^*, the observed data along with their sensor location $\mathcal{D}$ and the diffusion step k. Two binary masks manage missing data: one for features at observed locations and another for target locations, with 1 denoting observed data and 0 denoting missing data. The model is trained to minimize the noise prediction loss:

$$\mathcal{L}(\theta) = \mathbb{E}_{X_0^* \sim q, \varepsilon \sim \mathcal{N}(0,\mathbf{I}), k \sim \text{Uniform}(1,\ldots,K)} \left[\|\varepsilon - \varepsilon_\theta(X_k^*, k, s^*, \mathcal{D})\|^2 \right] \tag{1}$$

The denoising model integrates three specialized encoders to model the complex dependencies in spatio-temporal data. These encoders are applied sequentially, with multiple layers of each to refine the representations, and the diffusion step k is embedded as a conditioning signal to guide the denoising process. The following subsections detail each component, the Fourier compression upgrade, and the training/inference pipeline.

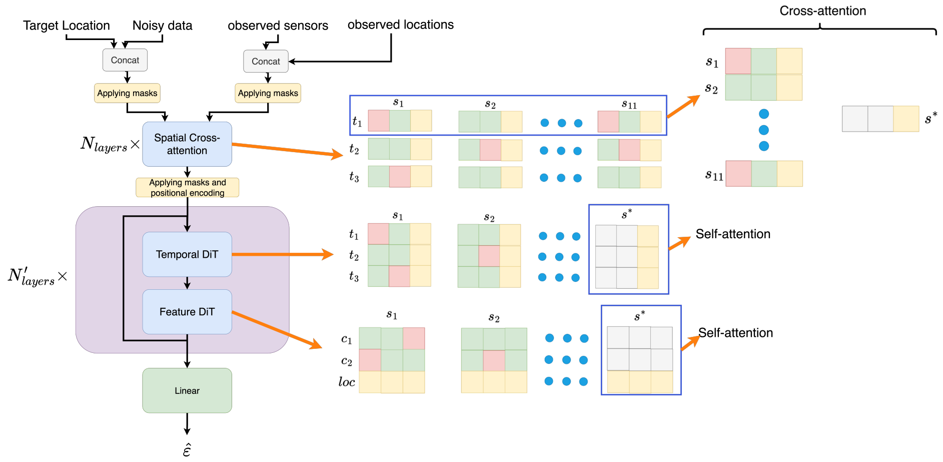

Figure 1: Overview of the model architecture when predicting the time-series data at one target location s^* (where there is no sensor) given 11 observed locations, each with two features. The green cells denote observed values at each sensor, red cells indicate missing entries, yellow cells store location metadata, and the grey cell represents a noisy placeholder for the target location's missing time series. The model applies spatial cross-attention on the observed sensors, followed by dedicated temporal and feature "DiT" modules, ultimately producing a prediction for the target location from the blended information of other neighbors.

4.2 Spatial Encoder

The Spatial Encoder models the spatial relationships between the target location s^* and the observed sensor locations, while incorporating the diffusion step k to condition the denoising process. To handle incomplete data, we incorporate missingness masks, which are binary indicators of whether a measurement is observed at a given (s, t), where $s \in \mathcal{S}, t \in \mathcal{T}$. For each time step $t \in \mathcal{T}$, we construct input data as follows:

Noisy Target Data: The target data at a particular time step $t \in \mathcal{T}$ and location $s^* \in \mathbb{R}^d$ is represented by the noisy sample $\mathbf{x}_k^* \in \mathbb{R}^C$, initialized as Gaussian noise at inference time. We concatenate $\mathbf{x}_k^*$ with the target location coordinates s^* and the corresponding missingness mask $\mathbf{m}^* \in \{0, 1\}^C$.

Conditional Observed Data: For each observed location $s \in \mathcal{S}$ and particular time step $t \in \mathcal{T}$, we concatenate the observed measurement $\mathbf{x} \in \mathbb{R}^C$, the location coordinates $s \in \mathbb{R}^d$, and the corresponding missingness mask $\mathbf{m} \in \{0, 1\}^C$.

The Spatial Encoder treats time steps as independent and identically distributed (IID) samples, allowing parallel computation across $\mathcal{T}$. The concatenated feature vectors for the noisy target and observed data are processed by a cross-attention mechanism, where the noisy target data serve as the query, and the observed sensor data serve as the key and value. This cross-attention computes attention weights that reflect the spatial relevance of each observed sensor to the target location, similar to the covariance-based weighting in kriging. The learnable weights within this module depend only on the combined size of feature vectors and location embedding rather than the number of locations, enabling the encoder to seamlessly handle a variable number of sensor locations. The spatial attention layers iteratively refine the representation, progressively integrating spatial information from neighboring sensors into the target predictions. We chose not to jointly model the spatial-temporal correlations to reduce the space, time, and sample complexities.

4.3 Temporal Encoder

Starting from the spatially contextualized target representation produced by the Spatial Encoder, the model refines it by capturing temporal and cross-feature correlations. The Temporal Encoder uses DiT (Peebles & Xie, 2023) self-attention to model temporal dependencies. We compute the self-attention on the target location only and treat the time dimension $\mathcal{T}$ as the sequence dimension.

Inputs are $X_k^* \in \mathbb{R}^{T\times C}$ for the target s^* and the conditional information for the observed locations. The diffusion step k is embedded with sinusoidal encodings and added to token embeddings to condition on the noise level. Self-attention operates along time (after temporal positional encodings), yielding a $T \times T$ attention map per location that captures temporal patterns across all features simultaneously. The number of learnable parameters for each layer is the sum of the feature dimension and the size of location embeddings. We concatenate the latter to inject spatial context.

4.4 Feature Encoder

Each Feature Encoder layer uses DiT blocks with self-attention. It models correlations among C features and injects spatial coordinate embeddings for spatial structure. We do this for the target location only. The feature dimension is treated as the sequence dimension. Parameters scale with the temporal dimension; conditional observed data provide context. The layer takes the output of the preceding Temporal Encoder. Self-attention computes feature-wise weights across all times at each location, learning dependencies between channels.

Temporal and Feature Encoders alternate–[Temporal → Feature]–repeated N'_{layers} times (a depth hyperparameter). This interleaving jointly models temporal-feature dependencies across levels. After the final Feature Encoder, we apply the DiT output head (Peebles & Xie, 2023) (LayerNorm + linear) to the target location to predict the noise.

4.5 Fourier compression (trend + seasonality) for DynaSTI

To mitigate DynaSTI's slow inference on long sequences, we compress each multivariate time-series (length L) into a compact trend + seasonality representation in the frequency domain as a truncated Fourier series (to lowest F frequency pairs). For feature k with centered time $\tau_t \in [-1, 1]$, we reconstruct:

$$\hat{y}_{t,k} = \underbrace{c_k + m_k\,\tau_t}_{\text{trend}} + \underbrace{\sum_{f=1}^{F}\Big[\alpha_{k,f}\cos\Big(\tfrac{2\pi f t}{L}\Big) + \beta_{k,f}\sin\Big(\tfrac{2\pi f t}{L}\Big)\Big]}_{\text{seasonality}}, \tag{2}$$

where the zero-th frequency component is absorbed by c_k. The *compressed vector* per feature is

$$\mathbf{z}_k = \big[\ \alpha_{k,1:F}\ ,\ \beta_{k,1:F}\ ,\ c_k\ ,\ m_k\ \big] \in \mathbb{R}^{2F+2}, \tag{3}$$

so a batch $y \in \mathbb{R}^{B\times L\times K}$ becomes $Z \in \mathbb{R}^{B\times(2F+2)\times K}$. In practice $2F+2 \ll L$, which yields faster diffusion steps despite a small coefficient-fitting overhead.

The diffusion model is trained directly on the compressed data. At each epoch, we map the observed conditionals to (α, β, c, m) by minimizing a reconstruction loss (a few gradient steps), then concatenate these coefficients to form Z. At inference, we apply the same mapping before running DynaSTI, reducing end-to-end latency relative to operating at length L. We initialize (c, m) via least squares on $(\tau_t, y_{\cdot,k})$, and set (α, β) by a one-shot real FFT of the series; all coefficients are subsequently refined by gradient descent. We are calling this model *FDynaSTI*.

4.6 Training & inference

Training: For each dataset, we partition the sensor locations into non-overlapping training and testing pools, with the training pool comprising 80% of the total locations. To ensure our model, DynaSTI, effectively handles incomplete data, we preserve any naturally occurring missing values in the training data. For datasets with minimal missing data, we introduce artificial missingness by randomly masking a subset of observations at the observed locations, enabling the model to learn to handle real-world scenarios with missing sensor data.

We train our model, DynaSTI, within the Denoising Diffusion Probabilistic Model (DDPM) framework, tailored for conditional generation of spatio-temporal data. At each training step, we uniformly sample a target location $s^* \in \mathcal{S}'$, where $\mathcal{S}' \subset \mathcal{S}$ is the training pool, with its true time-series data $X_0^* \in \mathbb{R}^{T\times C}$ (T time steps, C features). The conditional observed data $\mathcal{D}$ comprises time-series data $X_0 \in \mathbb{R}^{T\times C}$, and missingness masks $M \in \{0,1\}^{T\times C}$ for a set of observed

Table 2: Datasets Description

Dataset	Sampling interval	Time-series length	Number of features	Training locations	Testing locations
AWN	15 minutes	288 (3 days)	7	54	13
NACSE	1 day	30 days	2	143	36
METR-LA	5 minutes	288 (1 day)	1	165	42
PEMS-BAY	5 minutes	288 (1 day)	1	260	65

locations $\mathcal{S}_{\text{obs}} \subseteq \mathcal{S}' \setminus s^*$. We sample a diffusion step $k \sim \text{Uniform}(\{1, \ldots, K\})$ and noise $\varepsilon \sim \mathcal{N}(0, \mathbf{I})$, computing the noisy target data X_k^* according to Section 4.1. The model predicts the noise $\hat{\varepsilon} = \varepsilon_\theta(X_k^*, k, s^*, \mathcal{D})$, minimizing the loss in Eq. 1.

We explore two approaches to select $\mathcal{S}_{\text{obs}}$: (1) using all locations in $\mathcal{S}' \setminus s^*$ as observed sensors in each epoch; (2) randomly sampling a variable-sized subset of $\mathcal{S}' \setminus s^*$ per epoch, simulating dynamic sensor availability. Experiments show that both approaches yield comparable performance, but we adopt the first approach for training because of its simplicity throughout the paper.

Inference: During inference, the model starts with Gaussian noise $X_K^* \in \mathbb{R}^{T \times C} \sim \mathcal{N}(0, \mathbf{I})$ at the target location s^* and iteratively applies the reverse diffusion process conditioned on the target location s^*, diffusion step k, and conditional observed data along with locations $\mathcal{D}$:

$$X_{k-1}^* \sim p_\theta(X_{k-1}^* \mid X_k^*, k, s^*, \mathcal{D}), \quad k = K, K-1, \ldots, 1.$$

In each diffusion step k, we get the estimated noise $\hat{\varepsilon} = \varepsilon_\theta(X_k^*, k, s^*, \mathcal{D})$ and calculate the posterior mean and variance of the $(k-1)$-th step noisy target data $\mu_{k-1} = \frac{1}{\sqrt{\bar{\alpha}_k}}(X_k^* - \frac{\beta_k}{\sqrt{1-\bar{\alpha}_k}}\hat{\varepsilon})$ and $\sigma_{k-1} = \frac{1-\bar{\alpha}_{k-1}}{1-\bar{\alpha}_k}\beta_k$ respectively. Then, we get $X_{k-1}^* = \mathcal{N}(\mu_{k-1}, \sigma_{k-1}\mathbf{I})$ and repeat this procedure, decrementing k until $k = 1$, at which point we recover our prediction for the target location X_0^*.

5 Evaluation

In this section, we evaluate the performance of our proposed diffusion-based generative model for multivariate spatio-temporal data interpolation. We conduct experiments on four real-world datasets and compare our model against the following baseline methods based on their availability and handling multivariate data: (1) Deterministic methods: Mean imputation, DeepKriging (Nag et al., 2023), KITS (Li et al., 2023), GSLI (Yang et al., 2025), and IGNNK (Wu et al., 2021), (2) Probabilistic methods: ST-VGP (Hamelijnck et al., 2021), ImputeFormer (Nie et al., 2024), and PriSTI (Liu et al., 2023). Additionally, we perform an ablation study to assess the contribution of each component in our architecture.

5.1 Experimental setup

We utilize four diverse spatio-temporal datasets to evaluate our model. **AWN** dataset consists of weather data collected from the AgWeatherNet network [1] such as temperatures at two different pressure levels, relative humidity, dewpoint, wind speed, wind gust, and solar radiation. **NACSE** dataset provides daily maximum and minimum temperature data from 179 weather stations in Northwest Oregon, sourced from the NACSE PRISM climate dataset [2]. **METR-LA** and **PEMS-BAY** traffic datasets contain traffic speed data collected at 5-minute intervals from Los Angeles and San Francisco Bay Area (He, 2025) respectively. Table 2 shows the attributes of the four datasets.

Across datasets, we partition locations into disjoint train/test pools. In each trial, we sample a test location s^*, input its coordinates along with training-pool's locations and observations $\mathcal{D}$, and use s^*'s multivariate time-series as ground truth. We enforce a strict temporal split—train on earlier data, test on the final 20%—for all methods except ST-VGP (Hamelijnck et al., 2021). As a Gaussian Process method, ST-VGP's kernel trained on earlier windows extrapolates poorly under temporal shift, so a disjoint split would unfairly penalize it. We therefore fit ST-VGP on observations from the evaluation period–matching the test window of other methods–and predict the held-out targets,

[1] https://weather.wsu.edu/

[2] https://shorturl.at/Aor04

Table 3: Comparison of the RMSE (± 95% confidence interval) across four datasets

Model	NACSE	AWN	METR-LA	PEMS-BAY
MEAN	0.4113 ± 0.0590	0.9826 ± 0.0117	1.4954 ± 0.0269	0.9927 ± 0.0646
DeepKriging	0.8965 ± 0.0777	0.5651 ± 0.0142	1.3310 ± 0.0555	0.9524 ± 0.0842
ST-VGP	0.6408 ± 0.0133	0.5121 ± 0.0183	1.1577 ± 0.0442	0.8990 ± 0.0333
KITS	0.4009 ± 0.0251	0.4453 ± 0.0171	1.1502 ± 0.0425	0.8542 ± 0.0391
GSLI	0.6215 ± 0.0125	0.4567 ± 0.0145	1.1521 ± 0.0450	0.8406 ± 0.0534
IGNNK	0.8542 ± 0.0224	0.5400 ± 0.0139	1.3217 ± 0.0538	0.9446 ± 0.0986
PriSTI	0.5904 ± 0.0574	0.4766 ± 0.0171	1.1824 ± 0.0553	0.8762 ± 0.0930
ImputeFormer	0.3521 ± 0.0777	0.4436 ± 0.0181	1.1433 ± 0.0725	0.8432 ± 0.0629
DynaSTI	**0.2333 ± 0.0760**	0.4339 ± 0.0163	1.1216 ± 0.0687	0.8252 ± 0.0963
FDynaSTI	0.2608 ± 0.0597	**0.3706 ± 0.0186**	**1.0338 ± 0.0338**	**0.7996 ± 0.0522**

Table 4: Comparison of the CRPS and MIS (± 95% confidence interval) across four datasets

Model	NACSE		AWN		METR-LA		PEMS-BAY	
	CRPS	MIS	CRPS	MIS	CRPS	MIS	CRPS	MIS
ST-VGP	0.2351 ± 0.0521	15.21 ± 0.67	0.3211 ± 0.0230	7.32 ± 0.07	0.8532 ± 0.3320	10.78 ± 0.20	0.8245 ± 0.0341	15.65 ± 0.42
PriSTI	0.2740 ± 0.0477	23.46 ± 0.94	0.3542 ± 0.0121	12.71 ± 0.23	0.9777 ± 0.0355	13.43 ± 0.03	0.9573 ± 0.0886	19.18 ± 0.02
DynaSTI	**0.1631 ± 0.0515**	**11.17 ± 0.86**	0.2790 ± 0.0098	4.37 ± 0.15	0.6839 ± 0.0350	6.85 ± 0.46	**0.6392 ± 0.0308**	9.12 ± 0.72
FDynaSTI	0.1933 ± 0.0436	13.22 ± 0.87	**0.2440 ± 0.0110**	**2.17 ± 0.11**	**0.6528 ± 0.0049**	**5.58 ± 0.59**	0.6832 ± 0.0361	**7.74 ± 0.80**

a setup that favors ST-VGP. For each experiment, we run 10 trials per time period, varying the target location s^* to assess robustness across different spatial configurations.

We evaluate using RMSE at target locations, CRPS, and MIS. All metrics are reported as the mean with 95% confidence intervals over 10 runs. CRPS and MIS are probabilistic scoring rules (lower is better) that assess uncertainty quality—rewarding calibrated, sharp distributions and penalizing over- or under-confident predictions.

5.2 Results

We evaluate our model's performance across diverse scenarios, including virtual sensors and dynamic sensor configurations. In addition, we conducted an ablation study to evaluate the contribution of each of the key architectural components. Given that features vary in scale, we calculate the RMSE, CRPS, and MIS using normalized predictions and ground truth values.

Across all four datasets, our approach attains the best RMSE in Table 3. The Fourier variant (FDynaSTI) outperforms DynaSTI in all datasets except NACSE, which has relatively short time series. Relative to the strongest baseline model per dataset, the error reductions are 16.8% (AWN against KITS), 41.8% (NACSE against KITS), 10.1% (METR-LA against KITS), and 4.9% (PEMS-BAY against GSLI). These gains hold within the reported 95% confidence intervals.

DynaSTI/FDynaSTI achieves the lowest CRPS and MIS on all datasets in Table 4, indicating better-calibrated and sharper predictive distributions. For CRPS, FDynaSTI closely matches DynaSTI on METR-LA (0.6528 vs. 0.6839) and outperforms all on AWN, while DynaSTI leads on PEMS-BAY and NACSE (lower CRPS is better). In terms of MIS, FDynaSTI achieves the best performance across all datasets except NACSE, for which DynaSTI performs best. Note that deterministic baselines are omitted since CRPS and MIS does not apply to them.

To test the impact of dynamic sensor failures or sensor dropouts during inference, we gradually masked the input sensors randomly at inference time and show the results in Table 5 and performance degrades gracefully. From 100% to 10% active sensors, RMSE increases are +14.2% (AWN), +61.7% (NACSE), +85.6% (METR-LA), and +24.3% (PEMS-BAY), reflecting dataset difficulty while preserving competitive accuracy under severe sparsity.

Table 6 presents the results of an ablation study, where we remove key components of our model–Spatial Encoder (SE), Temporal Encoder (TE), and Feature Encoder (FE)–to assess their individual contributions. The Spatial Encoder is critical for maintaining model performance. Removing it more than doubles error on AWN and yields large degradations on NACSE, METR-LA, and PEMS-BAY. Removing the Temporal Encoder hurts notably on NACSE and METR-LA. The Feature Encoder

Table 5: Evaluation of our model's performance (RMSE ± 95% confidence interval) under varying percentages of active input sensors during inference

Dataset	**Percentage of Active Input Sensors**					
	100%	**90%**	**70%**	**50%**	**30%**	**10%**
AWN	0.3706 ± 0.0186	0.3770 ± 0.0195	0.3872 ± 0.0303	0.3860 ± 0.0173	0.4101 ± 0.0189	0.4231 ± 0.0190
NACSE	0.2333 ± 0.0760	0.2560 ± 0.0931	0.2868 ± 0.0995	0.3291 ± 0.0987	0.3302 ± 0.1021	0.3772 ± 0.1102
METR-LA	1.0338 ± 0.0338	1.1922 ± 0.0525	1.3132 ± 0.0566	1.5083 ± 0.0474	1.8231 ± 0.1607	1.9191 ± 0.1404
PEMS-BAY	0.7996 ± 0.0522	0.8292 ± 0.0942	0.8878 ± 0.0926	0.9232 ± 0.0974	0.9421 ± 0.0912	0.9938 ± 0.0983

Table 6: Ablation study on the four datasets. Each cell reports RMSE (± 95% confidence interval). SE: Spatial Encoder, TE: Temporal Encoder, FE: Feature Encoder.

Dataset	**DynaSTI/FDynaSTI**	**no SE**	**no TE**	**no FE**	**no TE & no FE**
AWN	$\mathbf{0.3706 \pm 0.0186}$	0.7836 ± 0.0067	0.3737 ± 0.0171	0.4192 ± 0.0069	0.4209 ± 0.0049
NACSE	$\mathbf{0.2333 \pm 0.0760}$	0.4462 ± 0.0749	0.3512 ± 0.0726	0.3376 ± 0.0784	0.3628 ± 0.0779
METR-LA	$\mathbf{1.0338 \pm 0.0338}$	1.7701 ± 0.0788	1.4086 ± 0.0774	N/A	N/A
PEMS-BAY	$\mathbf{0.7996 \pm 0.0522}$	1.1156 ± 0.1036	1.0124 ± 0.0417	N/A	N/A

matters for multivariate datasets (AWN and NACSE), while it is inapplicable to the two univariate traffic datasets. For both Table 5 and Table 6, we reported the RMSE values for the best performing model in Table 3, i.e., FDynaSTI for AWN, METR-LA, and PEMS-BAY, and DynaSTI for NACSE.

Table 7: Inference time (seconds) for each model to predict the entire time series at a single virtual sensor location on each of the four datasets.

Dataset	**DynaSTI**	**FDynaSTI**	**IGNNK**	**ST-VGP**	**DeepKriging**	**PriSTI**	**KITS**	**GSLI**
AWN	168.025s	28.920s	0.003s	2.211s	1.224s	59.708s	0.003	0.004s
NACSE	59.264s	39.357s	0.001s	0.025s	0.419s	26.603s	0.001	0.001s
METR-LA	200.374s	24.880s	0.002s	3.231s	1.445s	33.999s	0.002	0.002s
PEMS-BAY	292.911s	32.466s	0.003s	3.570s	1.256s	52.151s	0.003	0.003s

Table 7 shows the inference speeds of different models. Not surprisingly, the deterministic models are much faster than the generative models. FDynaSTI is significantly faster than DynaSTI and the other diffusion model, PriSTI. However it is slower than the other generative model, ST-VGP. We experimented with replacing the DDPM design of DynaSTI with DDIM (Song et al., 2020); however, we found that it significantly degrades the quality of the generated samples. All experiments were conducted on a cluster using GPU-enabled nodes equipped with Nvidia Tesla v100 32GB GPUs.

6 Discussion and Conclusions

Across four real-world datasets, DynaSTI delivers the best point accuracy (lowest RMSE, Table 3) and the best probabilistic quality (lowest CRPS, Table 4), showing that conditioning a diffusion model on spatial, temporal, and feature context yields both accurate means and well-calibrated, sharp uncertainty. The Fourier-compressed variant (FDynaSTI) outperforms or matches DynaSTI on several settings, offering faster sampling. Moreover, initializing harmonic coefficients with real FFT substantially improves accuracy over random starts (Appendix A.3, Table 9). DynaSTI is robust to time-varying sensor availability. As active sensors drop from 100% to 10%, errors rise gradually but remain competitive across datasets (Table 5). Ablations confirm the Spatial Encoder is critical (its removal more than doubles RMSE on AWN and NACSE), while Temporal and Feature encoders provide complementary gains (Table 6).

In summary, our proposed model significantly advances spatio-temporal interpolation by delivering a flexible, efficient, and accurate solution specifically designed to handle the complexities of real-world sensor networks. Its ability to manage missing data, adapt to changing configurations, and provide probabilistic predictions makes it a useful tool for applications such as environmental monitoring and traffic analysis. Moreover, as a generative model, it opens avenues for generating synthetic data, which could be valuable for training other models or conducting simulations in data-scarce environments.

REFERENCES

Ahmed Ben Said and Abdelkarim Erradi. Spatiotemporal tensor completion for improved urban traffic imputation. *IEEE Transactions on Intelligent Transportation Systems*, 23(7):6836–6849, 2022. doi: 10.1109/TITS.2021.3062999.

George Edward Pelham Box and Gwilym Jenkins. *Time Series Analysis, Forecasting and Control*. Holden-Day, Inc., USA, 1990. ISBN 0816211043.

Andrea Cini, Ivan Marisca, and Cesare Alippi. Filling the g_ap_s: Multivariate time series imputation by graph neural networks. In *International Conference on Learning Representations*, 2022. URL https://openreview.net/forum?id=kOu3-S3wJ7.

N. Cressie. *Statistics for spatial data*. John Wiley & Sons, 1993.

Noel A. C. Cressie and Christopher K. Wikle. *Statistics for Spatio-Temporal Data*. Wiley, Hoboken, NJ, 2011. URL https://books.google.com/books/about/Statistics_for_Spatio_Temporal_Data.html?id=-kOC6D0DiNYC.

A. P. Dempster, N. M. Laird, and D. B. Rubin. Maximum likelihood from incomplete data via the em algorithm. *Journal of the Royal Statistical Society, Series B (Methodological)*, 39(1):1–38, 1977.

Yutong Feng, Qiongyan Wang, Yutong Xia, Junlin Huang, Siru Zhong, and Yuxuan Liang. Spatio-temporal field neural networks for air quality inference, 2024. URL https://arxiv.org/abs/2403.02354.

Evelyn Fix and Jr. Hodges, Joseph L. Discriminatory analysis: Nonparametric discrimination: Consistency properties. Technical Report Report No. 4, USAF School of Aviation Medicine, Randolph Field, Texas, February 1951. Project No. 21-49-004.

Yarin Gal and Zoubin Ghahramani. Dropout as a Bayesian approximation: Representing model uncertainty in deep learning. In *International Conference on Machine Learning (ICML)*, volume 48 of *Proceedings of Machine Learning Research*, pp. 1050–1059, 2016. URL https://proceedings.mlr.press/v48/gal16.pdf.

Albert Gu and Tri Dao. Mamba: Linear-time sequence modeling with selective state spaces, 2024. URL https://arxiv.org/abs/2312.00752.

Oliver Hamelijnck, M. W. Wilkinson, Niclas A. Loppi, Arno Solin, and Tile Damoulas. Spatio-temporal variational gaussian processes. In *Advances in Neural Information Processing Systems*, volume 34, pp. 17104–17117, 2021.

Hengyuan He. California traffic network datasets: Metr-la, pems-bay, pems04 and pems08 for traffic speed and flow analysis, 2025. URL https://dx.doi.org/10.21227/j49q-ch56.

Jonathan Ho, Ajay Jain, and Pieter Abbeel. Denoising diffusion probabilistic models. In H. Larochelle, M. Ranzato, R. Hadsell, M.F. Balcan, and H. Lin (eds.), *Advances in Neural Information Processing Systems*, volume 33, pp. 6840–6851. Curran Associates, Inc., 2020. URL https://proceedings.neurips.cc/paper_files/paper/2020/file/4c5bcfec8584af0d967f1ab10179ca4b-Paper.pdf.

Junfeng Hu, Yuxuan Liang, Zhencheng Fan, Hongyang Chen, Yu Zheng, and Roger Zimmermann. Graph neural processes for spatio-temporal extrapolation. In *Proceedings of the 29th ACM SIGKDD Conference on Knowledge Discovery and Data Mining*, KDD '23, pp. 752–763. ACM, August 2023. doi: 10.1145/3580305.3599372. URL http://dx.doi.org/10.1145/3580305.3599372.

Junfeng Hu, Xu Liu, Zhencheng Fan, Yuxuan Liang, and Roger Zimmermann. Towards unifying diffusion models for probabilistic spatio-temporal graph learning. In *Proceedings of the 32nd ACM International Conference on Advances in Geographic Information Systems*, SIGSPATIAL '24, pp. 135–146, New York, NY, USA, 2024. Association for Computing Machinery. ISBN 9798400711077. doi: 10.1145/3678717.3691235. URL https://doi.org/10.1145/3678717.3691235.

Mohammad Rafid Ul Islam, Prasad Tadepalli, and Alan Fern. Self-attention-based diffusion model for time-series imputation in partial blackout scenarios. *Proceedings of the AAAI Conference on Artificial Intelligence*, 39(17):17564–17572, Apr. 2025. doi: 10.1609/aaai.v39i17.33931. URL https://ojs.aaai.org/index.php/AAAI/article/view/33931.

Baoyu Jing, Dawei Zhou, Kan Ren, and Carl Yang. Causality-aware spatiotemporal graph neural networks for spatiotemporal time series imputation. In *Proceedings of the 33rd ACM International Conference on Information and Knowledge Management*, CIKM '24, pp. 1027–1037. ACM, October 2024. doi: 10.1145/3627673.3679642. URL http://dx.doi.org/10.1145/3627673.3679642.

Sanmukh R. Kuppannagari, Yao Fu, Chung Ming Chueng, and Viktor K. Prasanna. Spatio-temporal missing data imputation for smart power grids. In *Proceedings of the Twelfth ACM International Conference on Future Energy Systems*, e-Energy '21, pp. 458–465, New York, NY, USA, 2021. Association for Computing Machinery. ISBN 9781450383332. doi: 10.1145/3447555.3466586. URL https://doi.org/10.1145/3447555.3466586.

Jiajun Li, Wenjie Chen, Yujun Hu, and Guojun Song. Kits: Inductive spatio-temporal kriging with increment training strategy. *arXiv preprint arXiv:2311.02565*, 2023.

Jie Li, Dun Lan, Yongshun Gong, Long Zhao, Wenpeng Lu, Yuhai Zhao, Xiangjun Dong, and Xiaoming Wu. Missing traffic data imputation with a conditional diffusion framework. *Expert Systems with Applications*, 296:129140, 2026. ISSN 0957-4174. doi: https://doi.org/10.1016/j.eswa.2025.129140. URL https://www.sciencedirect.com/science/article/pii/S0957417425027575.

Mingzhe Liu, Han Huang, Hao Feng, Leilei Sun, Bowen Du, and Yanjie Fu. Pristi: A conditional diffusion framework for spatiotemporal imputation. In *2023 IEEE 39th International Conference on Data Engineering (ICDE)*, pp. 1927–1939, 2023. doi: 10.1109/ICDE55515.2023.00150.

Xihaier Luo, Wei Xu, Yihui Ren, Shinjae Yoo, and Balu Nadiga. Continuous field reconstruction from sparse observations with implicit neural networks, 2024. URL https://arxiv.org/abs/2401.11611.

Ivan Marisca, Andrea Cini, and Cesare Alippi. Learning to reconstruct missing data from spatiotemporal graphs with sparse observations. In S. Koyejo, S. Mohamed, A. Agarwal, D. Belgrave, K. Cho, and A. Oh (eds.), *Advances in Neural Information Processing Systems*, volume 35, pp. 32069–32082. Curran Associates, Inc., 2022. URL https://proceedings.neurips.cc/paper_files/paper/2022/file/cf70320e93c08b39b1b29a348097a376-Paper-Conference.pdf.

Georges Matheron. Principles of geostatistics. *Economic Geology*, 58(8):1246–1266, 1963. doi: 10.2113/gsecongeo.58.8.1246.

Pratik Nag, Ying Sun, and Brian J. Reich. Spatio-temporal deepkriging for interpolation and probabilistic forecasting. *Spatial Statistics*, 57:100773, October 2023. ISSN 2211-6753. doi: 10.1016/j.spasta.2023.100773. URL http://dx.doi.org/10.1016/j.spasta.2023.100773.

Tong Nie, Guoyang Qin, Wei Ma, Yuewen Mei, and Jian Sun. Imputeformer: Low rankness-induced transformers for generalizable spatiotemporal imputation. In *Proceedings of the 30th ACM SIGKDD Conference on Knowledge Discovery and Data Mining*, KDD '24, pp. 2260–2271. ACM, August 2024. doi: 10.1145/3637528.3671751. URL http://dx.doi.org/10.1145/3637528.3671751.

William Peebles and Saining Xie. Scalable diffusion models with transformers. In *Proceedings of the IEEE/CVF international conference on computer vision*, pp. 4195–4205, 2023.

Carl Edward Rasmussen and Christopher K. I. Williams. *Gaussian Processes for Machine Learning*. MIT Press, Cambridge, MA, 2006. ISBN 978-0-262-18253-9.

Feras Saad, Jacob Burnim, Colin Carroll, Brian Patton, Urs Köster, Rif A Saurous, and Matthew Hoffman. Scalable spatiotemporal prediction with bayesian neural fields. *Nature Communications*, 15(1):7942, 2024. doi: 10.1038/s41467-024-51477-5.

Shanthi Saubhagya, Chandima Tilakaratne, Pemantha Lakraj, and Musa Mammadov. A novel hybrid spatiotemporal missing value imputation approach for rainfall data: An application to the ratnapura area, sri lanka. *Applied Sciences*, 14(3):999, 2024.

Jiaming Song, Chenlin Meng, and Stefano Ermon. Denoising diffusion implicit models. *arXiv:2010.02502*, October 2020. URL https://arxiv.org/abs/2010.02502.

Yusuke Tashiro, Jiaming Song, Yang Song, and Stefano Ermon. Csdi: Conditional score-based diffusion models for probabilistic time series imputation. In M. Ranzato, A. Beygelzimer, Y. Dauphin, P.S. Liang, and J. Wortman Vaughan (eds.), *Advances in Neural Information Processing Systems*, volume 34, pp. 24804–24816. Curran Associates, Inc., 2021. URL https://proceedings.neurips.cc/paper_files/paper/2021/file/cfe8504bda37b575c70ee1a8276f3486-Paper.pdf.

Aabila Tharzeen, Sai Munikoti, Punit Prakash, Jungkwun Kim, and Balasubramaniam Natarajan. A general spatiotemporal imputation framework for missing sensor data. In *2023 IEEE Conference on Artificial Intelligence (CAI)*, pp. 55–58, 2023. doi: 10.1109/CAI54212.2023.00032.

Yuankai Wu, Dingyi Zhuang, Aurelie Labbe, and Lijun Sun. Inductive graph neural networks for spatiotemporal kriging. *Proceedings of the AAAI Conference on Artificial Intelligence*, 35(5): 4478–4485, May 2021. ISSN 2159-5399. doi: 10.1609/aaai.v35i5.16575. URL http://dx.doi.org/10.1609/aaai.v35i5.16575.

Xinyu Yang, Yu Sun, Xinyang Chen, Ying Zhang, and Xiaojie Yuan. Graph structure learning for spatial-temporal imputation: Adapting to node and feature scales. In *Proceedings of the AAAI Conference on Artificial Intelligence*, volume 39, pp. 959–967, 2025. doi: 10.1609/aaai.v39i1.32081.

Taeyoung Yun, Haewon Jung, and Jiwoo Son. Imputation as inpainting: Diffusion models for spatiotemporal data imputation. 2023.

Jichao Zhang, Fan Zhong, Gongze Cao, and Xueying Qin. St-gan: Unsupervised facial image semantic transformation using generative adversarial networks. In Min-Ling Zhang and Yung-Kyun Noh (eds.), *Proceedings of the Ninth Asian Conference on Machine Learning*, volume 77 of *Proceedings of Machine Learning Research*, pp. 248–263, Yonsei University, Seoul, Republic of Korea, 15–17 Nov 2017. PMLR. URL https://proceedings.mlr.press/v77/zhang17c.html.

Jing Zhang and Jing Wei. Multi-residual tensor completion for spatiotemporal data imputation. *Internet of Things*, 25:101114, 2024. ISSN 2542-6605. doi: https://doi.org/10.1016/j.iot.2024.101114. URL https://www.sciencedirect.com/science/article/pii/S2542660524000568.

Chuanpan Zheng, Xiaoliang Fan, Chunyu Wang, Jianqi Qi, Chun Chen, and Long Chen. INCREASE: Inductive graph representation learning for spatio-temporal kriging. In *Proceedings of the ACM Web Conference 2023 (WWW '23)*, pp. 2771–2780. ACM, 2023. doi: 10.1145/3543507.3583525.

A Appendix

A.1 LLM usage

We used ChatGPT to aid in writing. We used it only to shorten sentences and improve grammar.

A.2 Incompleteness of datasets

The four datasets we used have some original missing values. Table 8 shows the percentage of missing values inherent to them.

Table 8: Percentage of missingness in the four datasets

Dataset	Percentage of missingness (%)
NACSE	24.76
AWN	53.56
METR-LA	8.11
PEMS-BAY	0.003

A.3 Random vs real FFT initialization of Fourier coefficients

Empirically, random initialization of the seasonal (sine/cosine) coefficients performs substantially worse than *real FFT (rFFT)* initialization. Random coefficients correspond to an arbitrary spectrum that poorly reconstructs the series in the time domain at the start of training, forcing gradient descent to discover both amplitudes and phases from scratch. In contrast, rFFT initialization aligns the initial parameters with the dominant spectral content of the detrended signal, placing optimization near a good basin. As a result, rFFT initialization achieves lower error with far fewer epochs, whereas random initialization typically requires many more updates to reach a comparable minimum—undermining the intended end-to-end speedup of our Fourier-compressed diffusion pipeline. For a fair comparison and to preserve the diffusion model's overall speedup, the Fourier model under both initialization schemes was trained for the same number of epochs; results are shown in Table 9.

Table 9: FDynaSTI's Fourier transform random vs real FFT initialization

Dataset	FDynaSTI-random	FDynaSTI-rFFT
AWN	0.9889 ± 0.0071	**0.3706 ± 0.0186**
NACSE	0.5651 ± 0.0621	**0.2608 ± 0.0597**
METR-LA	1.1872 ± 0.0444	**1.0338 ± 0.0338**
PEMS-BAY	1.0481 ± 0.1094	**0.7996 ± 0.0522**

A.4 Hyperparameters

Tables 10, 11, 12, 13, 14, 15, and 16 record the hyperparameters used for the corresponding model and dataset. All hyperparameters were tuned via grid search over predefined candidate values.

Table 10: DynaSTI/FDynaSTI hyperparameters

Hyperparameter	NACSE	AWN	METR-LA	PEMS-BAY
Epoch	2000/800	1000/600	1000/600	1000/600
Lr	1.0e-4	1.0e-4	1.0e-3	1.0e-4
β_{start}	0.0001	0.0001	0.0001	0.0001
β_{end}	0.1	0.1	0.1	0.1
Diffusion steps	50	50	50	50
Spatial context embedding	128	128	128	256
Spatial encoder layers	4	4	4	4
Temporal & Feature encoder layers	4	4	4	4
FDynaSTI Fourier transform parameters				
iterations	200	100	100	100
Lr	0.001	0.01	0.01	0.01
F	7	16	16	16

Table 11: ST-VGP hyperparameters

Hyperparameter	NACSE	AWN	METR-LA	PEMS-BAY
Likelihood noise	2.0	2.0	1.0	1.0
Variance	1.0	1.0	0.5	1.0
Lengthscale	(0.001,0.1,0,1)	(0.001,0.2,0,2)	(0.01,0.3,0,3)	(0.01,0.2,0,2)
Lr Adam	0.001	0.001	0.001	0.001
Lr Newton	0.1	0.1	0.1	0.1
Epoch	300	500	500	600

Table 12: PriSTI hyperparameters

Hyperparameter	NACSE	AWN	METR-LA	PEMS-BAY
Epoch	2000	1000	1000	1000
Lr	1.0e-4	1.0e-4	1.0e-3	1.0e-4
β_{start}	0.0001	0.0001	0.0001	0.0001
β_{end}	0.1	0.1	0.1	0.1
Diffusion steps	50	50	50	50
Layers	4	4	4	4
Channels	64	32	64	64
Number of heads	8	8	8	8
Projection dim	16	16	16	16
Time embedding dim	128	128	128	128
Feature embedding dim	16	16	16	16

Table 13: KITS hyperparameters

Hyperparameter	NACSE	AWN	METR-LA	PEMS-BAY
Epoch	300	500	300	300
Lr	0.001	0.0001	0.001	0.001
Samples per epoch	5120	5120	5120	5120
Hidden layer dim	64	64	64	64

Table 14: GSLI hyperparameters

Hyperparameter	NACSE	AWN	METR-LA	PEMS-BAY
Epoch	100	200	200	300
Lr	0.001	0.001	0.001	0.001
Channels	128	64	64	64
Projection dim	128	64	64	64
Time embedding dim	128	128	128	128
Feature embedding dim	16	16	16	16
Number of heads	8	8	8	8

Table 15: IGNNK hyperparameters

Hyperparameter	NACSE	AWN	METR-LA	PEMS-BAY
Epoch	5000	2000	2000	3000
Lr	1.0e-4	1.0e-5	1.0e-4	1.0e-6
Embedding dim	128	256	512	256
Order	1	3	3	3

Table 16: DeepKriging hyperparameters

Hyperparameter	NACSE	AWN	METR-LA	PEMS-BAY
Epoch	500	600	700	700
Lr	1.0e-3	1.0e-3	1.e-4	1.0e-4

A.5 QUALITATIVE RESULTS

Figures 2 and 3 visualize interpolation at two NACSE stations held out as virtual targets. The red curve is ground truth; purple and blue are the posterior means from DynaSTI and FDynaSTI. Shaded bands (pink for DynaSTI, cyan for FDynaSTI) denote the $\pm 3\sigma$ envelopes from generated samples, quantifying predictive uncertainty. Each figure also includes a map of Spatial Encoder attention over observed stations, indicating which sensors contribute most to the target prediction. Blue represents more attention-weight and green represents less.

Figures 4 and 5 show results for two stations in the AWN dataset showing the results of DynaSTI and FDynaSTI for all seven features.

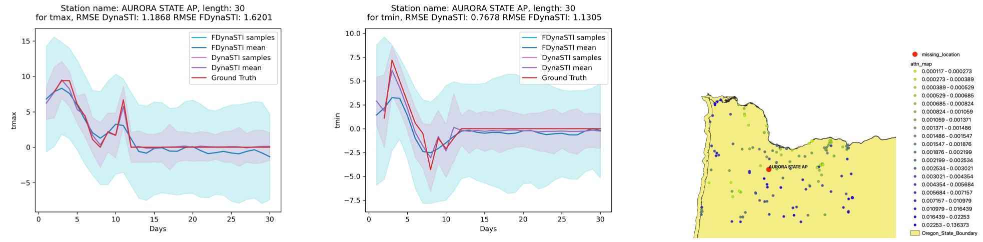

(a) Maximum temperature

(b) Minimum temperature

(c) Spatial encoder attention weights

Figure 2: NACSE dataset, missing station “Aurora State AP”

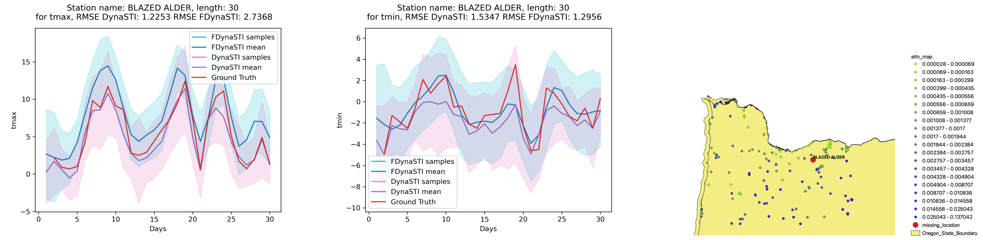

(a) Maximum temperature

(b) Minimum temperature

(c) Spatial encoder attention weights

Figure 3: NACSE dataset, missing station “Blazed Alder”

A.6 FDYNASTI FOURIER COEFFICIENT FITTING TIME

Table 17: Fourier coefficient fitting wall-clock time in seconds

Dataset	time (s)
NACSE	0.097
AWN	0.059
METR-LA	0.083
PEMS-BAY	0.071

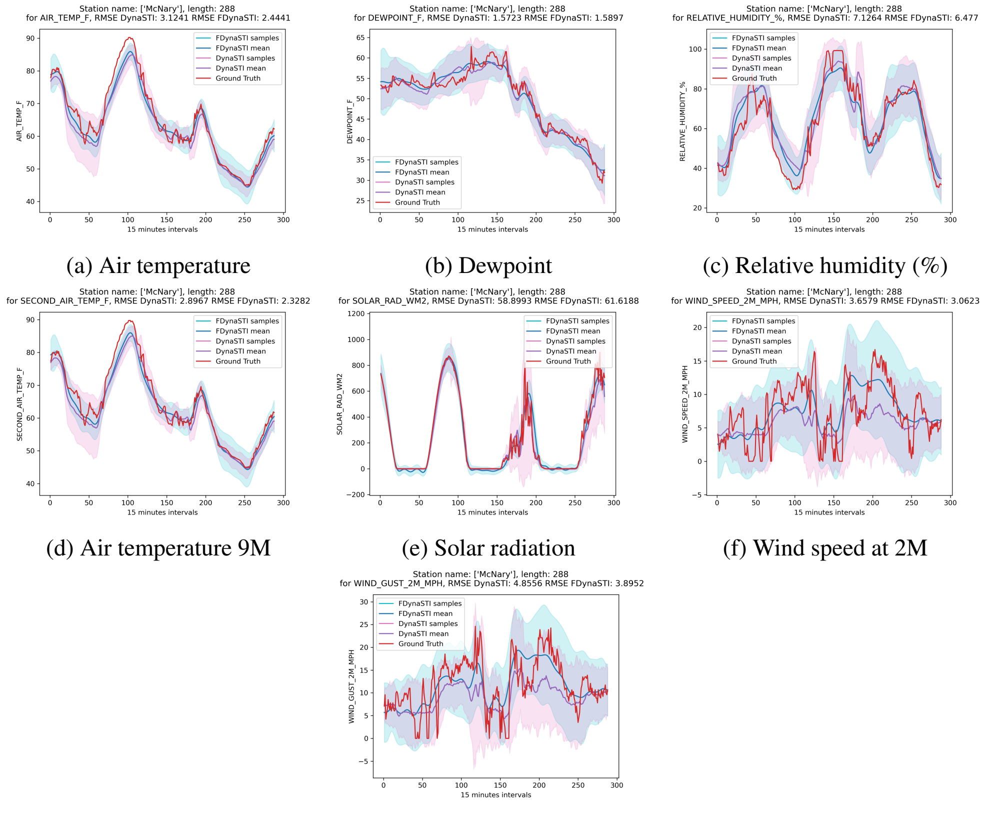

(a) Air temperature

(b) Dewpoint

(c) Relative humidity (%)

(d) Air temperature 9M

(e) Solar radiation

(f) Wind speed at 2M

(g) Wind gust at 2M

Figure 4: AWN dataset, missing station "McNary"

A.7 Training time comparison

Table 18 shows the training time comparison of all the models on all four datasets.

Table 18: Training time comparison of the models on all four datasets in d-hh:mm:ss format

Model	NACSE	AWN	METR-LA	PEMS-BAY
DeepKriging	00:20:12	01:08:31	01:58:09	02:07:57
ST-VGP	00:18:02	00:51:32	01:03:56	01:46:47
KITS	01:53:45	02:42:28	03:23:19	03:37:17
GSLI	00:15:10	00:37:42	01:10:23	01:22:34
IGNNK	00:21:47	01:17:13	02:12:30	02:19:14
PriSTI	00:58:52	03:59:15	06:32:38	06:56:29
ImputeFormer	00:26:21	01:21:42	02:10:24	02:18:57
DynaSTI	01:01:20	03:54:25	06:29:10	06:40:23
FDynaSTI	00:35:56	01:48:21	02:42:17	02:57:58

A.8 Sensitivity of F to loss and inference time

Figure 6 illustrates the sensitivity of FDynaSTI's performance to different values of F, while Figure 7 reports the corresponding inference times across all four datasets. As shown, increasing F generally reduces the loss but also leads to higher inference time. Therefore, as summarized in Table 10, we selected the final value of F by balancing this trade-off between accuracy and computational cost.

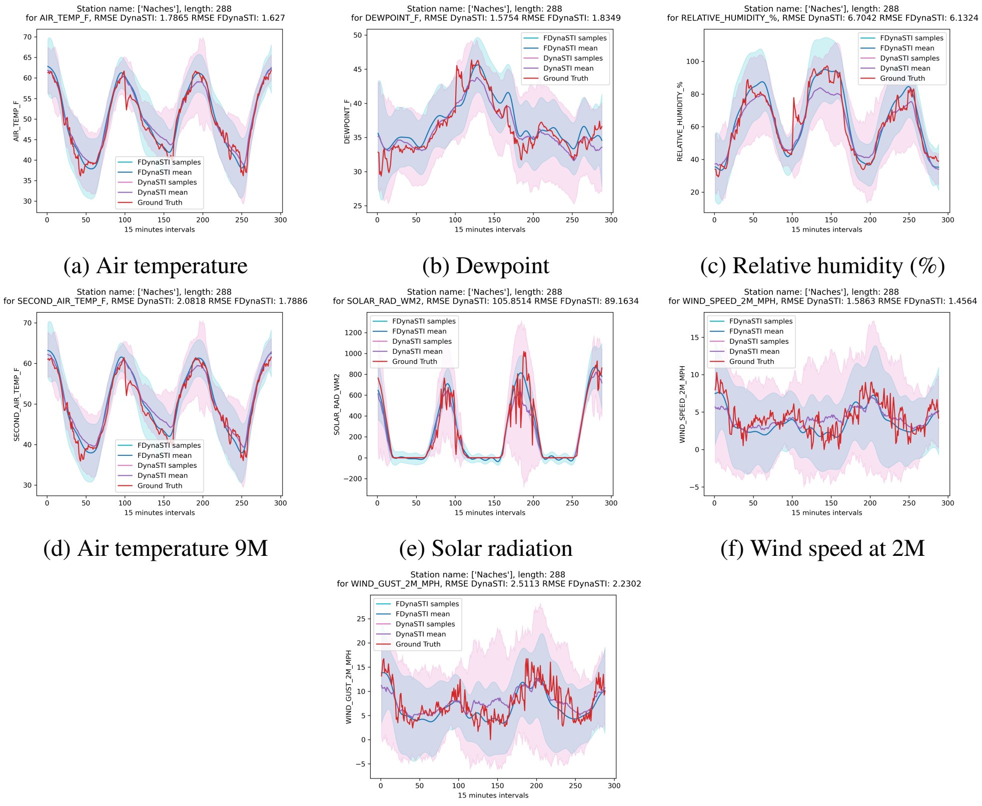

(a) Air temperature

(b) Dewpoint

(c) Relative humidity (%)

(d) Air temperature 9M

(e) Solar radiation

(f) Wind speed at 2M

(g) Wind gust at 2M

Figure 5: AWN dataset, missing station “Naches”

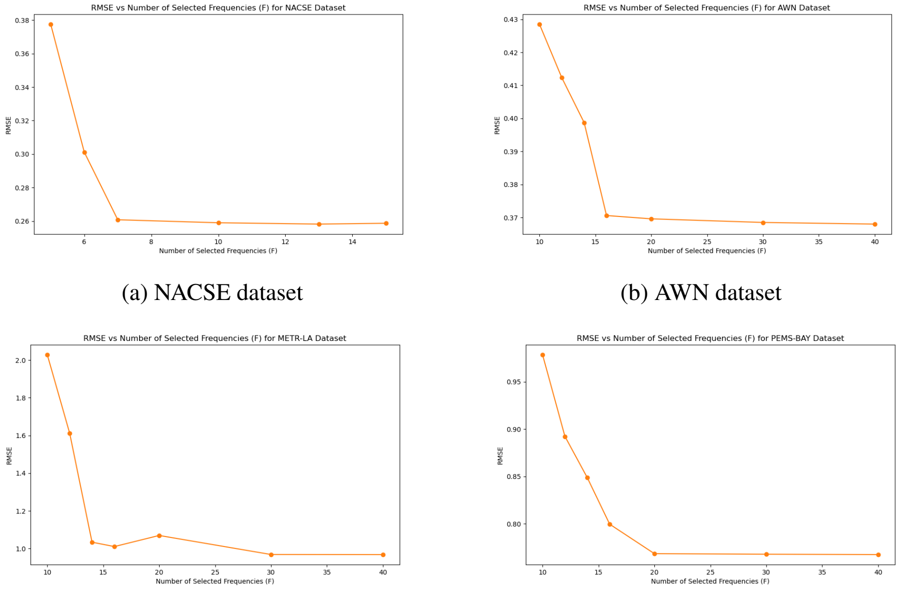

(a) NACSE dataset

(b) AWN dataset

(c) METR-LA dataset

(d) PEMS-BAY dataset

Figure 6: F vs RMSE of the FDynaSTI model for all four datasets

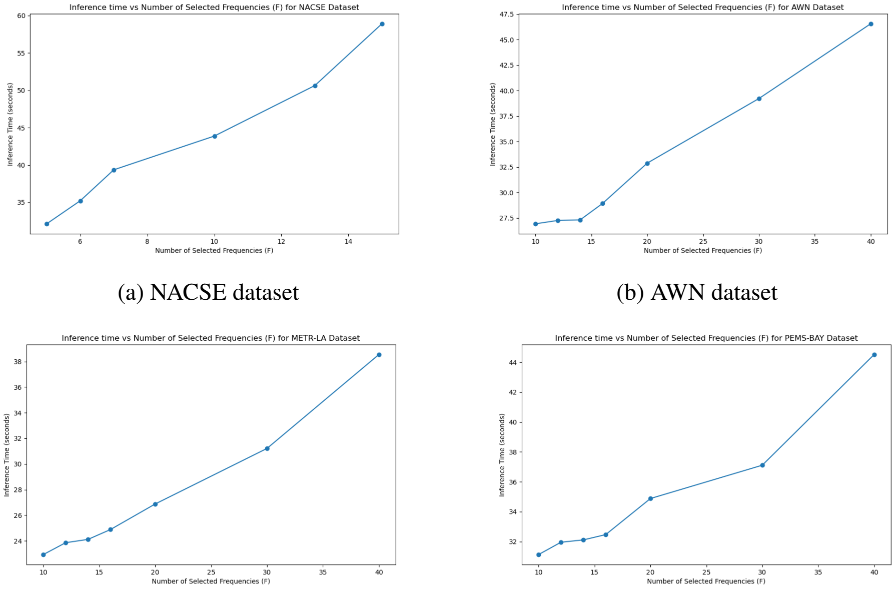

(a) NACSE dataset

(b) AWN dataset

(c) METR-LA dataset

(d) PEMS-BAY dataset

Figure 7: F vs inference time of the FDynaSTI model for all four datasets

A.9 Dataset visualization

The NACSE PRISM Climate dataset contains daily maximum and minimum temperatures from 176 weather stations in Northeast Oregon, recorded at 15-minute intervals from January 2011 to December 2021. For testing, we use the final two years of data.

The AgWeatherNet (AWN) dataset provides weather observations from 67 stations in Southeast Washington, spanning the period from 2007 to 2023. Each weather station contains features such as temperatures at two different pressure levels, relative humidity, dewpoint, wind speed, wind gust, and solar radiation.

The METR-LA dataset includes traffic speed measurements collected from 207 loop detectors installed across Los Angeles County highways. It covers a four-month period from March 1, 2012, to June 30, 2012.

The PeMS-Bay dataset, collected by Caltrans' Performance Measurement System (PeMS), contains traffic speed data from 325 sensors across the Bay Area. It covers six months of data from January 1 to May 31, 2017.

For all datasets, training and testing stations were randomly selected to form our experimental splits. Figure 8 illustrates the spatial distribution of the training and testing locations for each dataset.

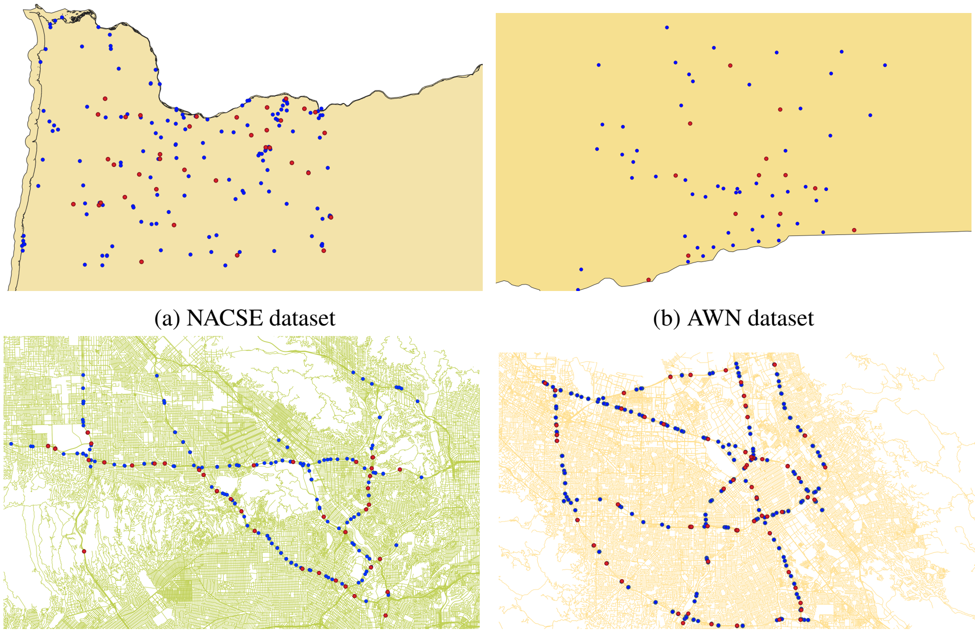
(a) NACSE dataset

(b) AWN dataset

(c) METR-LA dataset

(d) PEMS-BAY dataset

Figure 8: Training and testing location topology of all four datasets. The blue dots indicate training locations/sensors, and the red dots indicate testing locations/sensors.